Nascent adhesions differentially regulate lamellipodium velocity and persistence

Keith R. Carney[1,2], Akib M. Khan[1, 2], Shiela C. Samson[1, 2], Nikhil Mittal[3], Sangyoon J. Han[3], Michelle C. Mendoza[1,2,4]*⊥ and Tamara C. Bidone[4,5]*⊥

[1]Department of Oncological Sciences, University of Utah, Salt Lake City, UT

[2]Huntsman Cancer Institute, University of Utah, Salt Lake City, UT

[3]Department of Biomedical Engineering, Michigan Technological University, Houghton, MI

[4]Department of Biomedical Engineering, University of Utah, Salt Lake City, UT

[5]Scientific Computing and Imaging Institute, University of Utah, Salt Lake City, UT

* **Corresponding author:** Michelle Mendoza (michelle.mendoza@hci.utah.edu) and Tamara Bidone (tamarabidone@sci.utah.edu)

⊥ **Equal contribution**

Abstract

Cell migration is essential to physiological and pathological biology. Migration is driven by the motion of a leading edge, in which actin polymerization pushes against the edge and adhesions transmit traction to the substrate while membrane tension increases. How the actin and adhesions synergistically control edge protrusion remains elusive. We addressed this question by developing a computational model in which the Brownian ratchet mechanism governs actin filament polymerization against the membrane and the molecular clutch mechanism governs adhesion to the substrate (BR-MC model). Our model predicted that actin polymerization is the most significant driver of protrusion, as actin had a greater effect on protrusion than adhesion assembly. Increasing the lifetime of nascent adhesions also enhanced velocity, but decreased the protrusion's motional persistence, because filaments maintained against the cell edge ceased polymerizing as membrane tension increased. We confirmed the model predictions with measurement of adhesion lifetime and edge motion in migrating cells. Adhesions with longer lifetime were associated with faster protrusion velocity and shorter persistence. Experimentally increasing adhesion lifetime increased velocity but decreased persistence. We propose a mechanism for actin polymerization-driven, adhesion-dependent protrusion in which balanced nascent adhesion assembly and lifetime generates protrusions with the power and persistence to drive migration.

Keywords: actin polymerization, cell migration, computational model, lamellipodium, nascent adhesions

Introduction

Cell migration emerges from the controlled assembly of macromolecules that generate the mechanical forces of cell migration. Directional migration is specifically associated with the velocity and persistence of outward motion of the leading edge, termed lamellipodium protrusion [1, 2]. The edge protrusion is generated by actin filaments polymerizing against the plasma membrane and the formation of adhesions to the substrate [3, 4]. Actin polymerization generates pushing force that overcomes membrane tension and moves the cell edge forward [3, 5-7]. Counterforce from the membrane simultaneously induces actin retrograde flow away from the membrane and towards the cell center [7]. The actin retrograde flow becomes physically anchored to the substrate by adhesions, which transmit the flow to the substrate as traction force [8, 9]. Adhesion-mediated traction force promotes edge protrusion, but induces edge retraction if excessive [8, 10]. The pushing and traction forces are balanced for protrusive activity, but how the individual molecular dynamics generate this balance remains unknown.

Actin polymerization against the plasma membrane has been described as a stochastic Brownian ratchet [11]. In the Brownian ratchet model, fluctuations in the membrane and the actin filaments that abut the membrane create gaps between the two structures, which allow for the addition of new monomers that push against the leading edge [11]. The lamellipodium harbors an excess of monomeric actin that polymerizes onto existing filaments [7]. The actin nucleator ARP2/3 increases net actin polymerization by initiating new filaments off of the sides of existing filaments [12, 13]. Thus, ARP2/3 increases the number of actin filaments abutting and ratcheting against the membrane.

Fibroblasts and most epithelial cells move via cycles of edge protrusion, in which protrusions progress through protrusion initiation, reinforcement, and retraction phases that result from changes in membrane tension [14, 15]. Protrusions are initiated by the un-tethering of actin filaments from the membrane [16-18]. As the protrusion progresses, the membrane is stretched and membrane tension increases, which pushes back on the actin filaments and decreases the likelihood of new monomer addition [14, 19-21]. The mechanism by which filament elongation decreases with tension is explained by a force-velocity relationship in which actin filament elongation stalls at high force [22]. ARP2/3 activity increases after protrusion initiation in the reinforcement phase, which is also named the power phase in reference to the increased number of actin filaments pushing against the membrane [23-26]. Despite the increased pushing force, the mechanical feedbacks between membrane tension and actin polymerization cause edge velocity to slow after protrusion initiation.

The formation of small, transient adhesions in the lamellipodium, termed nascent adhesions, promotes and is required for protrusion velocity and persistence in protrusion-retraction cycles [27, 28]. Nascent adhesions work a molecular clutch, engaging and anchoring the actin filaments undergoing retrograde flow to the extracellular matrix on the substrate [3]. This decreases actin flow velocity [14, 29] and converts the motion into traction on the substrate and cell edge motion [30]. Because anchoring actin filaments onto adhesions also maintains the actin barbed ends against the membrane, the assembly rate of nascent adhesions correlates with leading edge velocity [31]. Molecular clutch disassembly depends on the amount of traction on the adhesions [14, 32]. Adhesion traction peaks along with the rate of actin retrograde flow in the reinforcement phase of edge protrusion [14, 24, 33]. The lifetime of nascent adhesions initially increases along with actin flow, but then decreases as actin flow increases further [10,

24], resulting in a stick and slip mechanism between actin filaments and adhesions. When nascent adhesions disassemble, they disengage from both the substrate and actin filaments [10].

The difficulty in experimentally isolating actin polymerization without affecting adhesion dynamics and vice versa has precluded a complete understanding of how lamellipodial actin polymerization and adhesion assembly and disassembly work together to control lamellipodium protrusion. In order to assess the contributions of actin and adhesion dynamics to edge motion, we developed a computational model that incorporates the Brownian ratchet mechanism (BR) and the molecular clutch mechanism (MC) [10, 34]. The model revealed that increasing the lifetime of adhesions supports cell edge velocity, but it reduces motional persistence in the initial phase of protrusion. Manipulation and computerized tracking of adhesion lifetime in live cells confirmed that adhesion lifetime promotes protrusion velocity but decreases motional persistence. Together, our findings suggest a previously unappreciated role for nascent adhesion force-dependent clutch mechanism in the control of initial leading-edge motion.

Results

We developed a novel computational model of lamellipodium protrusion based on Brownian dynamics. The model incorporates: explicit actin filaments represented as polar rods of interconnected units; nascent adhesions represented as dynamic point particles that link filaments to a fixed substrate; and a flexible membrane represented as a series of rigid rods connected by springs (Figure 1). We designed a 2D domain of 2 μm x 0.5 μm size, in which actin filaments fluctuate under thermal motion, polymerize, branch and depolymerize, and link to adhesions. Actin polymerization produces a force against the membrane ($\boldsymbol{F}_{Pol}$), which pushes the membrane forward. The displacement of the membrane produces an increase in membrane

tension ($\boldsymbol{F}_M$), which pushes the filaments away from the membrane and results in actin retrograde flow. $\boldsymbol{F}_M$ also decreases the actin polymerization rate according to the decreasing exponential force-velocity relation characteristic of the Brownian ratchet (BR) mechanism [11, 22, 35-37]. Filaments can link to substrate adhesions, which convert their retrograde flow into adhesion traction ($\boldsymbol{F}_A$). The model ensures force balance between $\boldsymbol{F}_{Pol}$, $\boldsymbol{F}_M$, and $\boldsymbol{F}_A$, resulting in relative movements of filaments and membrane at every time step (Figure 1A). The model simultaneously implements the Brownian ratchet mechanism of actin filament polymerization (BR) and the molecular clutch mechanism of adhesion dynamics (MC). The BR is implemented through the force-dependent velocity of filament elongation under membrane tension [11, 22, 35-37] (Figure 1B). The MC is implemented with biphasic force-dependent unbinding of adhesion clutches [38, 39] (Figure 1C).

The BR-MC model reproduces physiological lamellipodium motion

The BR-MC model produces continuous filament polymerization, filament branching against the membrane, and nascent adhesion assembly and disassembly. Membrane displacement, increased membrane tension after displacement, actin retrograde flow, and adhesion-mediated anchoring of the flow emerge from the molecular dynamics (Figure 2A and Figure 2 - movie supplement 1). We first tested that our model reproduces previous experimentally measured properties of the lamellipodium: edge motion velocity, actin retrograde flow velocity, and adhesion traction force [33, 40]. In order to verify how actin filament polymerization alone affects edge motion, we initially set membrane tension to k_m = 0.3 pN/nm, which is a value consistent with measurements in epithelial cells [41, 42]. We used a constant rate of actin filament branching (k_{branch} = 0.5 s^{-1}) that corresponds to experimentally measured

ARP2/3 activation [43], and a constant rate of adhesion unbinding (k_{off} = 0.1 s^{-1}) that matches the unloaded lifetime of integrin-ligand bonds [44-46]. We found that individual membrane segments exhibited initial velocity peaks of 30 - 40 nm/s and slower velocities as the protrusion progressed (Figure 2B). Within the corresponding segments of the lamellipodium, actin retrograde flow increased as the protrusion progressed (Figure 2C). Traction forces exhibited peaks of 60 - 80 pN (Figure 2D), consistent with experimental measurements of individual adhesions [32]. Plotting membrane and actin retrograde flow velocities as a function of traction force showed that membrane velocity increased and actin retrograde flow decreased as traction increased from 0 to 40 pN (Figure 2E), as previously described [30, 32].

We averaged the velocities and traction forces across the middle 1 μm membrane segment to mimic the computerized measurements from experimental images limited by the resolution of light microscopy. The mean protrusion velocity peaked at 24.3 nm/s at 10 s and slowed to 17.0 nm/s at 120 s (Figure 2 - figure supplement 1A), consistent with published measurements of PtK1 epithelial cells using (~25 nm/s [24, 33]). Actin retrograde flow increased after protrusion initiation, from a mean of 18.9 nm/s at 10 s to a mean of 26.7 nm/s at 120 s (Figure 2C and Figure 2 - figure supplement 1B), also consistent with PtK1 measurements (11.7 - 21.7 nm/s [24, 33]). The differences in time at which maximum edge velocity and maximum retrograde flow were reached are in quantitative agreement with the observed timing of lamellipodia actin retrograde in areas lacking significant traction force [24, 32, 33, 40].

We also validated the effects of membrane tension on the force relationships. In order to capture a greater range of edge velocity values, we modeled the nonmotile portion of membrane in cells by fixing the side boundaries of the modeling domain. Similar to our observations with unfixed edges, edge protrusion slowed and retrograde flow increased as the protrusion

progressed (Figure 2 –figure supplement 2A-B). Traction forces were stable, but high at the edges due to the high concentration of actin filaments and adhesions in the unstretched, tethered space (Figure 2 –figure supplement 2C). We ran the model with low membrane tension (0.03 pN/nm) to replicate the scenario of protrusion initiation and with high membrane tension (3 pN/nm) to represent the protrusion reinforcement phase [15, 30, 47]). We found that under low membrane tension, actin retrograde flow positively correlated with protrusion velocity (Figure 2 –figure supplement 2D). In contrast, under high membrane tension, actin retrograde flow negatively correlated with protrusion velocity (Figure 2 – figure supplement 2D). This is consistent with experimental data that shows high retrograde flow from the high rate of actin polymerization against the tense membrane, but slow protrusion velocity due to the high tension [20, 31, 32, 52].

Actin polymerization and adhesion assembly and disassembly control lamellipodium velocity

In order to decipher the contributions of actin filament polymerization and adhesion dynamics to membrane velocity, we systematically varied the rates of actin branching, adhesion assembly, and adhesion disassembly (k_{branch}, k_{on}, and k_{off}). For simplicity, we averaged the velocity of the 101 membrane segments, including the fixed edges of the modeling domain, which resulted in lower velocities than reported in Figure 2. We found that increasing k_{branch} four-fold (from 0.2 to 0.8 s^{-1}), with fixed adhesion assembly and disassembly rates (k_{on} = $k_{off,}$ = 0.1 s^{-1}), resulted in a 30% increase in protrusion velocity (from 16.6 nm/s to 21.5 nm/s, Figure 3A). Increasing adhesion assembly rate k_{on} five-fold (from 0.1 to 0.5 s^{-1}), with fixed k_{branch} = 0.5 s^{-1} and adhesion k_{off} = 0.3 s^{-1}, resulted in a 10% increase in protrusion velocity (from 17.8 nm/s to

19.6 nm/s, Figure 3B). Increasing the disassembly rate of adhesions five-fold decreased protrusion velocity 10% (from 19.8 nm/s to 18.4 nm/s, Figure 3C). Together, these results indicate that actin assembly is the main driver of edge velocity and that actin's control can be augmented by adhesion formation and lifetime. We tested how actin filament polymerization and adhesion dynamics together govern membrane motion by systematically varying k_{branch} and k_{off}. Membrane velocity increased with k_{branch} and decreased with k_{off} (Figure 3D). We also tested how adhesion formation and lifetime control protrusion velocity by simultaneously varying k_{on} and k_{off} and found that protrusion velocity peaks with the highest adhesion assembly rate and lowest adhesion disassembly rate (Figure 3E). This indicates that protrusion velocity depends on both adhesion assembly and maintenance. We found that the traction force transmitted by adhesions also peaked with the highest adhesion assembly rate and lowest adhesion disassembly rate, suggesting that adhesion traction force promotes edge protrusion (Figure 3F).

The lifetime of nascent adhesions regulates the velocity of the membrane

Adhesion traction determines the lifetime (τ) of adhesions, which is the inverse of unbinding rate ($\tau = 1/k_{off}$). To test the role of adhesion lifetime in protrusion, we incorporated a force-dependent molecular clutch mechanism into the computational model. The molecular clutch bases the probability of adhesion-actin bond breakage on tension and thus creates a variable rate of adhesion inactivation (k_{off}). We tested three different force-lifetime relations for the adhesions, varying for maximum lifetime, τ_{max} (Figure 4A). The breaking point for the actin-adhesion bond, or force corresponding to τ_{max}, was set at 30 pN [48-50]. The peaks in lifetime were either 3 s, 7.5 s, or 12 s, typical behavior of integrin unbinding from fibronectin

under load [48]. We used these force-lifetime relationships to control the probability of adhesion-actin bond breakage during simulations with variable actin polymerization rate. We found that membrane velocity increased proportionally with both k_{branch} and τ_{max} (Figure 4B). Increasing actin assembly 4-fold resulted in a 17% increase in edge velocity (from 13.3 to 15.6 nm/s, using $\tau_{max} = 3$ s), while increasing adhesion lifetime 4-fold resulted in about a 6% increase in velocity (from 15.6 to 16.5 nm/s, using k_{branch}= 0.8 s^{-1}). This result matched our findings on actin and adhesion-mediated control of edge motion in the absence of the molecular clutch (Figure 3D).

Increasing adhesion lifetime can have the secondary effect of increasing adhesion density, observed in Figure 3. Using k_{branch} = 0.5 s^{-1}, we found that increasing adhesion lifetime from 3 s to 12 s increased mean adhesion density from 299 to 505/μm^2 (Figure 4 – Figure Supplement 1A). We identified the range of allowed adhesions in simulations with τ_{max} = 3 s that would generate adhesion density of ~300 to 500/μm^2 (Figure 4 – Figure Supplement 1B). We then varied the maximum allowed adhesions to test how increasing adhesion density alone affects protrusion velocity, using the intermediate k_{branch} = 0.5 s^{-1}. We found that increasing mean adhesion density from 310 to 513/μm^2, independent of adhesion lifetime, increased protrusion velocity 2.3%, from 14.51 nm/s to 14.85 nm/s (Figure 4 – Figure Supplement 1C and D). Under the same conditions, increasing adhesion lifetime from 3 to 12 s resulted in a 4.6% increase in protrusion velocity, from 14.55 nm/s to 15.22 nm/s (Figure 4B and Figure 4 – Figure Supplement 1D). Thus, increased adhesion density resulting from increased lifetime does not fully explain adhesion lifetime's effects on edge velocity. These findings substantiate our conclusions that actin polymerization rate is the most significant driver of edge velocity and adhesion lifetime augments the velocity.

We evaluated the contribution of actin assembly and adhesion lifetime to pushing force on the membrane and the retrograde flow that results from membrane counterforce. We found that force on the membrane increased with both k_{branch} and τ_{max}, as peak force on the membrane occurred at the highest k_{branch} and τ_{max} (Figure 4C). Actin assembly was the main driver. With τ_{max} = 3 s, a four-fold increase in k_{branch} (from 0.2 – 0.4 s^{-1}) increased pushing force 21% (from 0.38 to 0.46 pN). With k_{branch} = 0.2 s^{-1}, four-fold increase in τ_{max} (from 3 – 12 s) increased pushing force 11% (from 0.38 to 0.42 pN). In contrast, actin retrograde flow increased with k_{branch} but decreased with τ_{max} (Figure 4D). The reduction in retrograde flow with adhesion lifetime is expected from previous experimental observations [14, 29]. These simulations with the τ_{max} variable suggest a critical role for the lifetime of nascent adhesions in regulating force against the membrane and the resulting edge velocity and actin retrograde flow.

The lifetime of nascent adhesions controls the persistence of membrane motion

Because pro-migratory signaling pathways promote the disassembly of nascent adhesions [53], which limited protrusion velocity in our model, we hypothesized that adhesion disassembly might promote the alternative edge protrusion output of protrusion persistence. We quantified protrusion persistence as the time between the large oscillations in membrane velocity, determined by Empirical Mode Decomposition (Figure 5 – figure supplement 1). While adhesion lifetime promoted protrusion velocity at low membrane tension (0.03 pN and 0.3 pN, Figure 5A and B), it decreased its motional persistence (Figure 5C and D). Under high tension, adhesion lifetime promoted membrane velocity without inhibiting persistence (Figure 5E and F). We tested the hypothesis that increasing the lifetime of nascent adhesions reduces protrusion persistence by slowing the motion of actin filaments and shortening the time it takes for actin

249 polymerization to stall. We computed the motion of actin filaments within 1 micron of
250 adhesions and varying τ_{max}. Increasing τ_{max} decreased the actin filaments' mean displacements
251 (Figure 5 – figure supplement 2A). Similarly, the time to stall, or decay time, for actin
252 polymerization decreased with increasing τ_{max} (Figure 5 – figure supplement 2B). Thus,
253 adhesion lifetime can decrease protrusion persistence by controlling actin filament mobility and
254 polymerization.
255
256 **Integrin activation promotes lamellipodium velocity and decreases its persistence**
257 To experimentally test the finding that adhesion lifetime promotes lamellipodia
258 protrusion velocity but limits persistence, we labeled adhesions in COS7 epithelial cells using
259 transient expression of Paxillin-mApple and imaged adhesion and edge dynamics during 5 min
260 of steady-state migration. We segmented the adhesions using focal adhesion analysis software
261 for quantification of the adhesions' lifetime [51] and used morphodynamics software to track the
262 edge motion [52] (Figure 6A and B). We noted that protrusions exhibited adhesions with
263 heterogeneous lifetimes, in which clusters of short-living adhesions co-resided with a few
264 longer-lifetime adhesions. The range of long lifetimes varied per movie, which appeared to be
265 related with edge protrusion. For example, a cell in which the longest lifetimes are ~4.7 min
266 (orange-colored adhesions in Figure 6A) showed slow, persistent progression of the cell edge
267 (Figure 6A). On contrary, a cell in which the longest lifetimes are ~10.6 min (yellow-colored
268 adhesions in Figure 6B) showed fast and more fluctuating protrusion behavior (Figure 6B).
269 Accordingly, we sampled the lifetimes of the top 1 percentile of long-living adhesions per movie
270 and obtained the corresponding protrusion velocities and persistent times of the closest edge
271 segments. Plotting edge velocity and persistence as a function of adhesion lifetime showed that

cell protrusions with longer mean adhesion lifetimes were associated with faster protrusion velocity but shortened protrusion persistence (Figure 6C and D).

We also treated COS7 cells with Mn^{+2}, which increases adhesion lifetime and density [44-46, 48]. Mn^{+2} stabilizes nascent adhesions by promoting integrins' structural shift to high-affinity conformations for binding to extracellular matrix [10, 53, 54]. The cells transiently expressed Emerald-Lifeact to label the cell edge. We imaged the cells' steady-state protrusion-retraction cycles and quantified protrusion velocity and persistence with morphodynamics software. We found that integrin activation with Mn^{+2} increased mean protrusion velocity but decreased persistence when compared to untreated cells (Figure 6E and F). Together, these results support our model that longer adhesion lifetimes are associated with faster protrusion velocity but reduced protrusion persistence.

Discussion

Using our novel particle-based BR-MC model, we discovered that actin polymerization is the main driver of lamellipodium velocity and that the force-dependent clutch mechanism of nascent adhesions differentially controls lamellipodium velocity and persistence. Experiments in migrating epithelial cells substantiated that nascent adhesion lifetime promotes protrusion velocity and limits persistence. Directional migration requires persistent edge motion [1, 2], which is optimal at intermediate extracellular matrix density and nascent adhesion concentration [55]. Our findings suggests that in addition to extracellular matrix density, the strength of the adhesion-actin interaction controls protrusion persistence.

Our study clarifies the contributions of lamellipodium actin polymerization and nascent adhesions to overall edge motion. Previous models have indicated both that actin polymerization

295 is sufficient to drive edge protrusion and that adhesion promotes protrusion [28, 31, 56-59]. In
296 the recent model by Garner et al., filament polymerization alone generated stable protrusion [60],
297 which resembles the lamellipodia of fish keratocytes that glide with a static cell shape [61]. Yet,
298 the density of adhesion activation has been shown to promote and be required for protrusion
299 velocity and persistence in protrusion-retraction cycles [28, 59]. We showed that increasing
300 actin polymerization most significantly enhances protrusion velocity and that increasing the
301 nascent adhesion lifetime further supports edge velocity through the molecular clutch
302 mechanism. However, we found that increasing nascent adhesion lifetime reduced the edge
303 motional persistence when membrane tension was moderate, as in the initiation phase of
304 membrane motion. In live cells cycling through the phases of protrusion initiation,
305 reinforcement, and retraction, nascent adhesion lifetime associated with and promoted
306 lamellipodium protrusion velocity but limited persistence. This suggests that the nascent-
307 adhesion mediated regulation in the beginning of edge protrusion dictates the overall protrusion
308 activity.

309 We propose a mechanism for nascent adhesion lifetime's differential control of edge
310 velocity and persistence: the increase in edge velocity emerges from the traction that the
311 adhesions exert on the substrate to convert actin retrograde flow into edge motion, while the
312 decrease in persistence arises from the force-velocity relation of actin filaments polymerizing
313 against the plasma membrane. In the initial phase of lamellipodium protrusion, increasing
314 adhesion lifetime tethers the actin filament tips in proximity of the edge, which supports actin
315 filament pushing against the membrane until membrane tension stalls polymerization. The
316 longer the time of filament anchoring, the faster this effect is reached, resulting in decreased
317 protrusion persistence with increasing τ_{max}. However, when membrane tension has increased,

318 such as at the end of the reinforcement phase, the increase in membrane tension that results from
319 polymerization is too nominal to affect the duration of actin filament polymerization. This
320 model, developed from our computational simulations, is supported by our experimental studies
321 and a complementary study in HT-1080 fibrosarcoma cells migrating slowly on aligned fibers of
322 extracellular matrix [62]. Our tracking of COS7 cell adhesion lifetime and edge motion found
323 that a few long-living adhesions govern edge protrusion. In the HT-1080 study, adhesion
324 lifetime was experimentally controlled by fiber orientation such that adhesions aligned with the
325 matrix had longer lifetimes and more persistent protrusions. When mature adhesions were
326 removed through inhibition of myosin II, the remaining nascent adhesions did not control
327 persistence. Rather, extracellular matrix fibers biased protrusion persistence along the fibers
328 through contact guidance [62].

329 Our BR-MC model revealed this critical and differential role of nascent adhesions in
330 supporting membrane motion because it incorporated the Brownian ratchet and molecular clutch
331 mechanisms without imposing feedback relations between the actin, adhesion, and membrane
332 dynamics. Prior models of lamellipodial protrusion at the sub micrometer length scale probed
333 the role of actin polymerization using the Brownian ratchet force-velocity relationship of actin
334 filament elongation pushing the membrane [60, 63, 64], or probed actin and adhesion
335 interactions by representing the actin as a gel with the molecular clutch adhesion lifetime-
336 traction force relationship [27, 28, 30]. However, none of the previous models [28, 56, 57, 65-
337 67], to the best of our knowledge, simultaneously incorporated the Brownian ratchet and
338 molecular clutch mechanisms without predetermined relations between membrane motion and
339 actin filament concentration or actomyosin contractility. In our model, lamellipodium dynamics
340 emerge spontaneously from interactions and force balance between actin filaments, membrane,

and adhesions. Because we focused on the roles of nascent adhesion dynamics and myosin-independent actin flow, the BR-MC model does not incorporate effects from load adaptations within the actin network or actomyosin contractility. Thus, we cannot exclude that membrane tension feedback to actin network geometry and density [68-71] or traction force feedback to actomyosin contractility and adhesion stabilization [29, 72] influences nascent adhesion regulation of protrusion. Nevertheless, our experiments in cells detected the model's relationship between adhesion lifetime on protrusion velocity and persistence. This suggests that nascent adhesions also drive lamellipodium velocity and limit persistence in the context of other complex interactions.

In summary, we establish an unexpected role for nascent adhesion lifetime in the differential regulation of protrusion velocity and persistence. We previously showed that integrin subunits have distinct flexibilities and conformations that affect the affinity and avidity of interaction with the matrix [73]. The resulting strength of the integrin-actin molecular clutch interaction controls adhesion lifetime, which controls lamellipodium actin assembly. Thus, while actin polymerization is needed for nascent adhesion formation in edge protrusion [29, 31], our findings indicate that integrin adhesions also control actin assembly. Future studies are needed to determine which integrin-extracellular matrix interactions promote intermediate adhesion lifetime for directed migration in heterogenous environments and how biochemical and mechanical signaling affects adhesion lifetime to alter cell migration.

Materials and Methods

Model of lamellipodium protrusions based on Brownian Ratchet and Molecular Clutch (BR-MC)

We developed a 2D model of lamellipodium protrusion based on combining the Brownian ratchet mechanism for actin filament polymerization against a cell edge [11, 22, 35, 37] with the molecular clutch mechanism for adhesions [38, 39]. The model domain is 2 μm x 0.5 μm rectangular domain, with a moving boundary at the top that mimics the flexible cell edge membrane (Figure 1A). Explicit elements in the domain are actin filaments modeled as rigid rods of interconnected units, a flexible membrane of 101 elastically interconnected units, and adhesions modeled as single point particles that create dynamic anchor points for the filaments. Within the domain, actin filaments fluctuate in Brownian motion, polymerize at their barbed ends, depolymerize at their pointed ends, create branches against the membrane and become capped. Actin filaments polymerize against the edge membrane at assembly rate k_{pol} and branching rate k_{branch}, which generates pushing force that induces outward membrane motion (Figure 1A). Integrins undergo cycles of activation and deactivation, which correspond to their addition to and removal from the simulation domain. These mechanisms are governed by kinetic rates (Table 1). Filaments and integrins interact by establishing potential energies, and filaments push the edge membrane by exerting force on it. The membrane motion increases membrane tension, $\boldsymbol{F}_M$, which results in retrograde flow of the actin filaments. Through the retrograde flow, the $\boldsymbol{F}_M$ is transmitted to the adhesions in the form of traction force. In response to the traction force, adhesions dynamically unbind at a force dependent rate, k_{off}. Displacements of actin filaments and membrane are calculated over the course of the simulation as a function of the forces acting on them, using the overdamped Langevin Equation as:

$$\frac{dr}{dt} = \frac{F_{TOT}}{\gamma}$$

where F_{TOT} is the sum of deterministic and stochastic forces, r is a position vector for the elements in the system, γ is the environment drag coefficient (assuming cytoplasm viscosity), and dt is the simulation time step. A complete description of the model, including the implementation scheme and relative interactions between actin, adhesions and membrane, is below.

Model initialization. During the initialization of the model, a membrane is placed on the top boundary and the actin filaments are randomly distributed within the domain. Each actin filament is initialized with a length of n units, with each unit representing 5 monomers or 15 nm. The n number of units is randomly selected from a normal distribution with a mean of 15, corresponding to an average filament length of 225 nm, a standard deviation of 2, and a minimum n of 1. The concentration of actin filaments is maintained at a steady state of 9000 filamentary units in the simulation domain. This creates a buildup of actin filaments during the first second of simulations, with the occasional addition of filaments thereafter in order to maintain a steady concentration of filaments.

A finite number of integrins are allowed to activate and deactivate according to their kinetic rates, until they reach a steady state concentration. Allowed adhesions = 1000 when simulations are run using a force-independent k_{off}. Allowed adhesions = 2000 with force-dependent k_{off}. The effective concentration of integrins emerges in the model from the relative magnitudes of k_{off} and k_{off}.

Model iterations. The model is developed using MATLAB R2020b, using the explicit Euler implementation scheme for performing each model iteration, which consists of kinetics,

force balance, and position updates. The kinetic events occur following sequential steps: polymerization, depolymerization, capping and branching of the actin filaments, and adhesion activation and deactivation. Then, interactions between actin filaments and membrane and between filaments and adhesions are evaluated and the corresponding forces are calculated. Last, based on the force balance between interacting elements, the relative positions between actin filaments and membrane, and between actin filaments and adhesions are calculated, and the boundary conditions applied.

Actin filament representation and dynamics. In the model, actin filaments are represented as rigid and polar rods of interconnected units (Figure 1A). Their polymerization occurs as addition of units at the filament barbed ends, with rate k_{polym}. Depolymerization occurs as removal of units from the pointed ends, at a rate $k_{depolym}$. Actin filaments within a branch window of 15 nm from the membrane can also form branches at a rate k_{branch}. Branching occurs as elongation of new filaments from existing (mother) filaments in the direction towards the membrane and at an angle θ relative to the mother filament. θ is randomly selected from a normal distribution with a mean of 70 deg and standard deviation of 10 deg. Filaments capping occurs at a rate k_{cap}, which stops filaments polymerization and branching.

Actin filament polymerization follows the Brownian ratchet mechanism. In order to account for the effects of membrane tension on actin filaments polymerization, filaments presenting barbed ends within 15 nm from the membrane slow their polymerization rate depending on the force on them. For these filaments, the probability of polymerization is calculated as $P_{polym} = C_p\, k_{polym}\, dt$, where the polymerization coefficient, C_p, varies between 0 and 1:

$$C_p = e^{-(F_M + F_B)/k_B T}$$

where F_M is membrane tension, F_B is a confining boundary which ensures a reflective boundary, and k_BT = 4.11 pN nm.

Actin filament connection to adhesions. When a filamentary unit is within a distance r_{thresh} from integrin, a harmonic interaction potential is established between the filament and integrin, with force: $F_A = r_{0,A}\, k_A$, where k_A is the integrin-filament spring constant, and $r_{0,A}$ is the distance from the equilibrium, resulting from actin retrograde flow. When an integrin switches its state from active to inactive, the connection with the actin filament is lost and integrin disappears.

Filament motion follows Langevin dynamics. The total force on each actin filaments is computed as: $F_{TOT} = F_T + F_A + F_M + F_B$, where F_T is a Brownian, stochastic force following the fluctuation dissipation theorem, F_A is the force from one or more bound integrins, F_M is the force exerted by the membrane, and F_B is the boundary force which acts as a repulsive potential preventing the filaments from crossing. When one filament presents one or more branches and/or branches on branches, the interconnected filaments are treated as a rigid structure.

Filaments positions are calculated over time following Langevin equation in the limit of high friction: $r_i(t) = r_i(t_0) + \frac{F_{TOT,i}}{\gamma_F} dt \quad for\ i = 1,2,3, \dots N$, where N is the total number of filaments and filament structures, γ_F is the frictional coefficient and dt is the simulation time step.

Integrin representation and dynamics. Integrins are represented as single point particles existing in two functional states: active or inactive, as they undergo cycles of activation and deactivation at rates k_{on} and k_{off}, respectively. When active, integrins are placed in random positions in the simulation domain and provide anchor points for filaments motion. When

inactive, they are removed from the domain. While integrin activation is governed by k_{on}, their de-activation occurs through one of two mechanisms: force-independent or force-dependent unbinding. In the first case, k_{off} has a constant value (Table 1). In the second case, k_{off} depends biphasically on the tension between actin filament and integrin, F_A. According to the catch-bond model for integrin unbinding, the unbinding rate is a sum of two exponentials with opposite signs (Figure 4A):

$$k_{off} = Ae^{as_1F_A} + Be^{bs_2F_A}$$

Three lifetimes versus force relations were used in the model (lifetime $\tau = 1/k_{off}$) and they are here referenced according to their maximum τ values (τ_{max}):

	$\tau_{max} = 3$	$\tau_{max} = 7.5$	$\tau_{max} = 12$
A	2.0	0.5	0.25
B	0.5E-5	0.5E-5	0.5E-5
a	-9.727E-3	-7.286E-3	-6.12E-3
b	0.3	0.3	0.3
s_1	6.8	6.8	6.8
s_2	1.0405	0.9228	0.8606

Membrane representation and dynamics. The edge membrane is represented with consecutive rigid rods, each 18 nm long, interconnected by harmonic interaction potentials of stiffness k_m and equilibrium separation $r_{0,M}$. Each membrane segment experiences two forces: the filaments pushing against it, and the pulling from neighboring membrane segments.

Over the course of the simulations, positions of membrane segments are updated following the Langevin equation, as: $r_s(t) = r_s(t_0) + \left(F_{pol,s} + F_{M,s}\right)\frac{dt}{\gamma_M}$ *for s = 1,2,3,…101,* where F_{pol} is the force from filaments, and F_M is the elastic force contribution from the connection with neighboring membrane segments. γ_F is the drag coefficient from the fluid in front of the membrane (outside the cell).

468 Determination of traction force. Mean traction force is the average of all adhesion-
469 filament connections over all time points and positions. All force values greater the 500 pN
470 resulted from motion too fast for the 1 ms timestep and were excluded (F_A < 500 pN).

471 Extraction of protrusion persistence. Velocity data for each membrane segment was
472 decomposed into its Intrinsic Mode Functions (IMF) using Empirical Mode Decomposition. The
473 first 7 IMFs were subtracted so that thermal noise oscillations in membrane velocity were on the
474 scale of real cell protrusion oscillations, in which change in velocity is at least 5 nm/s (Figure 5 -
475 figure supplement 1).

476

Key resources table

Reagent type (species or resource)	Designation	Source or reference	Identifiers	Additional Information
Cell line *(Chlorocebus sabaeus)*	COS7	ATCC	CCL-81.2	
Transient expression vector	pcDNA3-mApple Paxillin	Smith et al. 2013 PMID: 23990882		Dr. Mary Beckerle (University of Utah, Salt Lake City, UT)
Transient expression vector	mEmerald-Lifeact	Addgene	#54148	Emerald-Lifeact-7

Cell culture

COS7 cells were obtained from ATCC, cultured in Dulbecco's Modified Eagle Medium (DMEM) with 4.5 g/L D-glucose, L-glutamine, and sodium pyruvate (Gibco 11965092) containing 5% Fetal Bovine Serums (FBS, Avantor Seradigm 97068-085), and tested for micoplasma every 3-6 months. Micoplasma-negative COS7 cells were plated on acid-treated 1.5 coverslips within 35 mm glass-bottom dishes (MatTek P35G-1.5-14-C), and transfected the following day with pcDNA3.1/Paxillin-mApple or mEmerald-Lifeact at 20% confluency using TransIT-LT1 (Mirus MIR 2304) following the manufacturer's instructions. Two days post-transfection, medium was replaced with FluoroBrite DMEM (Gibco #) supplemented with 10% FBS and 20 mM HEPES.

Live cell TIRF imaging of adhesions

For adhesion imaging, cells were imaged on an automated Nikon Ti inverted microscope with motorized total internal reflection fluorescence (TIRF), Perfect Focus 3 to maintain laser-

493 based identification of the bottom of the substrate during acquisition, a CFI Apo TIRF 100x oil
494 Apo 1.49 NA objective, 561 solid-state laser (Vortran), ET620/60m emission filter (Chroma),
495 and Photometrics Prime 95B camera configured at a 100 MHz readout speed to decrease readout
496 noise with Metamorph. Images were taken every 3 s for 5 min, with sequential images at every
497 time point with the TIRF angle set to optimal TIRF and with the TIRF angle set as vertical for
498 effective widefield imaging. The acquired images had an effective pixel size of 45 nm. Imaging
499 was performed at 37°C, 5% carbon dioxide, and 70% humidity. Laser powers were decreased as
500 much as possible and the exposure time set at 200-400 ms to avoid phototoxicity.
501

502 **Adhesion segmentation, detection, and tracking**

503 Nascent adhesions were detected and segmented using point source detection as
504 previously described in [51, 74]. Briefly, fluorescence images were filtered using the Laplacian
505 of Gaussian filter and then local maxima were detected. Each local maximum was then fitted
506 with an isotropic Gaussian function (standard deviation: 2.1 pixels, i.e. ~180 nm) and outliers
507 were removed using a goodness of fit test (p=0.05). The point sources detected for nascent
508 adhesions were tracked over the entire frames of the time-lapse images using uTrack [75].
509 Lifetimes of adhesions were calculated from lifetimes of individual tracked trajectories. A GUI-
510 based MATLAB software for the edge analysis is from Danuser lab [52]. Due to the noise in
511 edge motion from the 3 s framerate, IMFs were removed in the edge motion data.
512

513 **Live cell confocal imaging of cell edge and analysis**

514 For cell edge imaging, cells expressing mEmerald-Lifeact were imaged on a Nikon Ti
515 inverted microscope with a CFI Apo TIRF 60x oil, 1.45 NA objective employing Perfect Focus,

a Yokagawa CSU-10 spinning disk confocal with Spectral Applied Research Borealis modification, a 488 solid-state laser, Chroma ET525/50m filter, and Photometrics Myo CCD camera with Metamorph. Images were taken every 10 s for 5 min, with 400-700 ms exposures. For experiments with prolonged adhesion lifetime, cells were treated with 1 mM $MnCl_2$ 2 h prior to imaging. Time-lapse images were analyzed for cell edge protrusion dynamics in MATLAB software as described previously [76]. A GUI-based MATLAB software for the edge analysis is from Danuser lab [52]. A two-sample nonparametric Kolmogorov–Smirnov test at 5% significance tested for population distribution equality. IMFs were not removed from this edge motion data.

Statistics

Models were run until additional iterations no longer changed the result output. The non-parametric Mann-Whitney U test was used to test for difference in the means for all modeling data and adhesion-edge analyses. Experiment sample size was chosen based on a minimum of three independent biological replicates and hundreds to thousands of adhesions and protrusion events analyzed, respectively, within each replicate. The Kolmogorov-Smirnov test was used to test for difference in the distribution of edge motion upon Mn^{+2} treatment. Unless otherwise mentioned in each figure caption, * $p<0.05$, ** $p<0.01$, *** $p<0.001$, **** $p<0.0001$.

Software availability

MATLAB software for the computational model is shared via GitHub at https://github.com/KRCSLC/ProtrusionModel.

A GUI-based MATLAB software for the adhesion analysis is shared via GitHub at https://github.com/HanLab-BME-MTU/focalAdhesionPackage.git; Han, 2021; copy archived at swh:1:rev:6aeb3593a5fd3ace9b0663d1bf0334decfb99835.

Acknowledgements

Thanks to Drs. Mark Smith and Mary Beckerle for the gift of pcDNA3-mPaxillin-mApple. Thanks to Dr. Drew Elliott for acquisition of the timelapse images of Paxillin-mApple in COS7 cells. Thanks to the University of Utah Cell Imaging Core and the University of Utah Center for High Performance Computing. The work was supported by funding from the National Science Foundation NSF-BMMB-2044394 to T.B.D., the Huntsman Cancer Institute and Scientific Computing and Imaging Institute CORI to T.B.D., American Cancer Society RSG CSM130435 to M.C.M. and National Institutes of Health 1R15GM135806 to S.J.H.

Competing Interests

The authors declare no competing interests.

References

1. Harms, B.D., et al., *Directional persistence of EGF-induced cell migration is associated with stabilization of lamellipodial protrusions.* Biophys J, 2005. **88**(2): p. 1479-88.
2. Riaz, M., et al., *Persistence of fan-shaped keratocytes is a matrix-rigidity-dependent mechanism that requires alpha5beta1 integrin engagement.* Sci Rep, 2016. **6**: p. 34141.
3. Gardel, M.L., et al., *Mechanical integration of actin and adhesion dynamics in cell migration.* Annu Rev Cell Dev Biol, 2010. **26**: p. 315-33.
4. Pollard, T.D. and G.G. Borisy, *Cellular motility driven by assembly and disassembly of actin filaments.* Cell, 2003. **112**(4): p. 453-65.
5. Abraham, V.C., et al., *The actin-based nanomachine at the leading edge of migrating cells.* Biophys J, 1999. **77**(3): p. 1721-32.
6. Lacayo, C.I., et al., *Emergence of large-scale cell morphology and movement from local actin filament growth dynamics.* PLoS Biol, 2007. **5**(9): p. e233.
7. Pollard, T.D., *Regulation of actin filament assembly by Arp2/3 complex and formins.* Annu Rev Biophys Biomol Struct, 2007. **36**: p. 451-77.
8. Giannone, G., et al., *Periodic lamellipodial contractions correlate with rearward actin waves.* Cell, 2004. **116**(3): p. 431-43.
9. Hu, K., et al., *Differential transmission of actin motion within focal adhesions.* Science, 2007. **315**(5808): p. 111-5.
10. Oakes, P.W., et al., *Lamellipodium is a myosin-independent mechanosensor.* Proc Natl Acad Sci U S A, 2018. **115**(11): p. 2646-2651.
11. Mogilner, A. and G. Oster, *Force generation by actin polymerization II: the elastic ratchet and tethered filaments.* Biophys J, 2003. **84**(3): p. 1591-605.
12. Achard, V., et al., *A "primer"-based mechanism underlies branched actin filament network formation and motility.* Curr Biol, 2010. **20**(5): p. 423-8.
13. Mullins, R.D., J.A. Heuser, and T.D. Pollard, *The interaction of Arp2/3 complex with actin: nucleation, high affinity pointed end capping, and formation of branching networks of filaments.* Proc Natl Acad Sci U S A, 1998. **95**(11): p. 6181-6.
14. Ji, L., J. Lim, and G. Danuser, *Fluctuations of intracellular forces during cell protrusion.* Nat Cell Biol, 2008. **10**(12): p. 1393-400.
15. Prass, M., et al., *Direct measurement of the lamellipodial protrusive force in a migrating cell.* J Cell Biol, 2006. **174**(6): p. 767-72.
16. Bisaria, A., et al., *Membrane-proximal F-actin restricts local membrane protrusions and directs cell migration.* Science, 2020. **368**(6496): p. 1205-1210.
17. Mogilner, A. and G. Oster, *Cell motility driven by actin polymerization.* Biophys J, 1996. **71**(6): p. 3030-45.
18. Welf, E.S., et al., *Actin-Membrane Release Initiates Cell Protrusions.* Dev Cell, 2020. **55**(6): p. 723-736 e8.
19. Gauthier, N.C., et al., *Temporary increase in plasma membrane tension coordinates the activation of exocytosis and contraction during cell spreading.* Proc Natl Acad Sci U S A, 2011. **108**(35): p. 14467-72.
20. Houk, A.R., et al., *Membrane tension maintains cell polarity by confining signals to the leading edge during neutrophil migration.* Cell, 2012. **148**(1-2): p. 175-88.
21. Raucher, D. and M.P. Sheetz, *Cell spreading and lamellipodial extension rate is regulated by membrane tension.* J Cell Biol, 2000. **148**(1): p. 127-36.

22. Brangbour, C., et al., *Force-velocity measurements of a few growing actin filaments.* PLoS Biol, 2011. **9**(4): p. e1000613.
23. Amann, K.J. and T.D. Pollard, *The Arp2/3 complex nucleates actin filament branches from the sides of pre-existing filaments.* Nat Cell Biol, 2001. **3**(3): p. 306-10.
24. Lee, K., et al., *Functional hierarchy of redundant actin assembly factors revealed by fine-grained registration of intrinsic image fluctuations.* Cell Syst, 2015. **1**(1): p. 37-50.
25. Suraneni, P., et al., *The Arp2/3 complex is required for lamellipodia extension and directional fibroblast cell migration.* J Cell Biol, 2012. **197**(2): p. 239-51.
26. Wu, C., et al., *Arp2/3 is critical for lamellipodia and response to extracellular matrix cues but is dispensable for chemotaxis.* Cell, 2012. **148**(5): p. 973-87.
27. Shemesh, T., et al., *Role of focal adhesions and mechanical stresses in the formation and progression of the lamellipodium-lamellum interface [corrected]*. Biophys J, 2009. **97**(5): p. 1254-64.
28. Welf, E.S., H.E. Johnson, and J.M. Haugh, *Bidirectional coupling between integrin-mediated signaling and actomyosin mechanics explains matrix-dependent intermittency of leading-edge motility.* Mol Biol Cell, 2013. **24**(24): p. 3945-55.
29. Alexandrova, A.Y., et al., *Comparative dynamics of retrograde actin flow and focal adhesions: formation of nascent adhesions triggers transition from fast to slow flow.* PLoS One, 2008. **3**(9): p. e3234.
30. Zimmermann, J., et al., *Actin filament elasticity and retrograde flow shape the force-velocity relation of motile cells.* Biophys J, 2012. **102**(2): p. 287-95.
31. Choi, C.K., et al., *Actin and alpha-actinin orchestrate the assembly and maturation of nascent adhesions in a myosin II motor-independent manner.* Nat Cell Biol, 2008. **10**(9): p. 1039-50.
32. Gardel, M.L., et al., *Traction stress in focal adhesions correlates biphasically with actin retrograde flow speed.* J Cell Biol, 2008. **183**(6): p. 999-1005.
33. Mendoza, M.C., et al., *ERK reinforces actin polymerization to power persistent edge protrusion during motility.* Sci Signal, 2015. **8**(377): p. ra47.
34. Bidone, T.C., et al., *Multiscale model of integrin adhesion assembly.* PLoS Comput Biol, 2019. **15**(6): p. e1007077.
35. Carlsson, A.E., *Growth of branched actin networks against obstacles.* Biophys J, 2001. **81**(4): p. 1907-23.
36. Carlsson, A.E., *Growth velocities of branched actin networks.* Biophys J, 2003. **84**(5): p. 2907-18.
37. Schaus, T.E. and G.G. Borisy, *Performance of a population of independent filaments in lamellipodial protrusion.* Biophys J, 2008. **95**(3): p. 1393-411.
38. Chan, C.E. and D.J. Odde, *Traction dynamics of filopodia on compliant substrates.* Science, 2008. **322**(5908): p. 1687-91.
39. Elosegui-Artola, A., et al., *Mechanical regulation of a molecular clutch defines force transmission and transduction in response to matrix rigidity.* Nat Cell Biol, 2016. **18**(5): p. 540-8.
40. Ponti, A., et al., *Two distinct actin networks drive the protrusion of migrating cells.* Science, 2004. **305**(5691): p. 1782-6.
41. Lieber, A.D., et al., *Membrane tension in rapidly moving cells is determined by cytoskeletal forces.* Curr Biol, 2013. **23**(15): p. 1409-17.

42. Shi, Z. and T. Baumgart, *Membrane tension and peripheral protein density mediate membrane shape transitions.* Nat Commun, 2015. **6**: p. 5974.
43. Beltzner, C.C. and T.D. Pollard, *Pathway of actin filament branch formation by Arp2/3 complex.* J Biol Chem, 2008. **283**(11): p. 7135-44.
44. Gailit, J. and E. Ruoslahti, *Regulation of the fibronectin receptor affinity by divalent cations.* J Biol Chem, 1988. **263**(26): p. 12927-32.
45. Mould, A.P., S.K. Akiyama, and M.J. Humphries, *Regulation of integrin alpha 5 beta 1-fibronectin interactions by divalent cations. Evidence for distinct classes of binding sites for Mn2+, Mg2+, and Ca2+.* J Biol Chem, 1995. **270**(44): p. 26270-7.
46. Smith, J.W., R.S. Piotrowicz, and D. Mathis, *A mechanism for divalent cation regulation of beta 3-integrins.* J Biol Chem, 1994. **269**(2): p. 960-7.
47. Parekh, S.H., et al., *Loading history determines the velocity of actin-network growth.* Nat Cell Biol, 2005. **7**(12): p. 1219-23.
48. Kong, F., et al., *Demonstration of catch bonds between an integrin and its ligand.* J Cell Biol, 2009. **185**(7): p. 1275-84.
49. Yao, M., et al., *Mechanical activation of vinculin binding to talin locks talin in an unfolded conformation.* Sci Rep, 2014. **4**: p. 4610.
50. Yeoman, B., et al., *Adhesion strength and contractility enable metastatic cells to become adurotactic.* Cell Rep, 2021. **34**(10): p. 108816.
51. Han, S.J., et al., *Pre-complexation of talin and vinculin without tension is required for efficient nascent adhesion maturation.* Elife, 2021. **10**.
52. Machacek, M. and G. Danuser, *Morphodynamic profiling of protrusion phenotypes.* Biophys J, 2006. **90**(4): p. 1439-52.
53. Kamata, T., et al., *Membrane-proximal {alpha}/{beta} stalk interactions differentially regulate integrin activation.* J Biol Chem, 2005. **280**(26): p. 24775-83.
54. Lin, G.L., et al., *Activation of beta 1 but not beta 3 integrin increases cell traction forces.* FEBS Lett, 2013. **587**(6): p. 763-9.
55. Cirit, M., et al., *Stochastic model of integrin-mediated signaling and adhesion dynamics at the leading edges of migrating cells.* PLoS Comput Biol, 2010. **6**(2): p. e1000688.
56. MacKay, L., E. Lehman, and A. Khadra, *Deciphering the dynamics of lamellipodium in a fish keratocytes model.* J Theor Biol, 2021. **512**: p. 110534.
57. Atilgan, E., D. Wirtz, and S.X. Sun, *Morphology of the lamellipodium and organization of actin filaments at the leading edge of crawling cells.* Biophys J, 2005. **89**(5): p. 3589-602.
58. Gov, N.S. and A. Gopinathan, *Dynamics of membranes driven by actin polymerization.* Biophys J, 2006. **90**(2): p. 454-69.
59. Shemesh, T., A.D. Bershadsky, and M.M. Kozlov, *Physical model for self-organization of actin cytoskeleton and adhesion complexes at the cell front.* Biophys J, 2012. **102**(8): p. 1746-56.
60. Garner, R.M. and J.A. Theriot, *Leading edge stability in motile cells is an emergent property of branched actin network growth.* bioRxiv, 2020: p. 2020.08.22.262907.
61. Lee, J., A. Ishihara, and K. Jacobson, *The fish epidermal keratocyte as a model system for the study of cell locomotion.* Symp Soc Exp Biol, 1993. **47**: p. 73-89.
62. Kubow, K.E., et al., *Contact guidance persists under myosin inhibition due to the local alignment of adhesions and individual protrusions.* Sci Rep, 2017. **7**(1): p. 14380.

63. Ditlev, J.A., et al., *An open model of actin dendritic nucleation.* Biophys J, 2009. **96**(9): p. 3529-42.
64. Lee, K.C. and A.J. Liu, *Force-velocity relation for actin-polymerization-driven motility from Brownian dynamics simulations.* Biophys J, 2009. **97**(5): p. 1295-304.
65. Huber, F., J. Kas, and B. Stuhrmann, *Growing actin networks form lamellipodium and lamellum by self-assembly.* Biophys J, 2008. **95**(12): p. 5508-23.
66. Craig, E.M., et al., *Membrane tension, myosin force, and actin turnover maintain actin treadmill in the nerve growth cone.* Biophys J, 2012. **102**(7): p. 1503-13.
67. Rubinstein, B., K. Jacobson, and A. Mogilner, *Multiscale Two-Dimensional Modeling of a Motile Simple-Shaped Cell.* Multiscale Model Simul, 2005. **3**(2): p. 413-439.
68. Batchelder, E.L., et al., *Membrane tension regulates motility by controlling lamellipodium organization.* Proc Natl Acad Sci U S A, 2011. **108**(28): p. 11429-34.
69. Bieling, P., et al., *Force Feedback Controls Motor Activity and Mechanical Properties of Self-Assembling Branched Actin Networks.* Cell, 2016. **164**(1-2): p. 115-127.
70. Mueller, J., et al., *Load Adaptation of Lamellipodial Actin Networks.* Cell, 2017. **171**(1): p. 188-200 e16.
71. Rutkowski, D.M. and D. Vavylonis, *Discrete mechanical model of lamellipodial actin network implements molecular clutch mechanism and generates arcs and microspikes.* PLoS Comput Biol, 2021. **17**(10): p. e1009506.
72. Bachir, A.I., K.E. Kubow, and A.R. Horwitz, *Fluorescence fluctuation approaches to the study of adhesion and signaling.* Methods Enzymol, 2013. **519**: p. 167-201.
73. Bidone, T.C., et al., *Coarse-Grained Simulation of Full-Length Integrin Activation.* Biophys J, 2019. **116**(6): p. 1000-1010.
74. Han, S.J., et al., *Traction microscopy to identify force modulation in subresolution adhesions.* Nat Methods, 2015. **12**(7): p. 653-6.
75. Jaqaman, K., et al., *Robust single-particle tracking in live-cell time-lapse sequences.* Nat Methods, 2008. **5**(8): p. 695-702.
76. Samson, S.C., et al., *p90 ribosomal S6 kinase (RSK) phosphorylates myosin phosphatase and thereby controls edge dynamics during cell migration.* J Biol Chem, 2019. **294**(28): p. 10846-10862.
77. Wiseman, P.W., et al., *Spatial mapping of integrin interactions and dynamics during cell migration by image correlation microscopy.* J Cell Sci, 2004. **117**(Pt 23): p. 5521-34.
78. Vallotton, P., et al., *Recovery, visualization, and analysis of actin and tubulin polymer flow in live cells: a fluorescent speckle microscopy study.* Biophys J, 2003. **85**(2): p. 1289-306.
79. Pollard, T.D., *Rate constants for the reactions of ATP- and ADP-actin with the ends of actin filaments.* J Cell Biol, 1986. **103**(6 Pt 2): p. 2747-54.
80. Schafer, D.A., P.B. Jennings, and J.A. Cooper, *Dynamics of capping protein and actin assembly in vitro: uncapping barbed ends by polyphosphoinositides.* J Cell Biol, 1996. **135**(1): p. 169-79.
81. Footer, M.J., et al., *Direct measurement of force generation by actin filament polymerization using an optical trap.* Proc Natl Acad Sci U S A, 2007. **104**(7): p. 2181-6.
82. Kovar, D.R. and T.D. Pollard, *Insertional assembly of actin filament barbed ends in association with formins produces piconewton forces.* Proc Natl Acad Sci U S A, 2004. **101**(41): p. 14725-30.

83. Svitkina, T.M. and G.G. Borisy, *Arp2/3 complex and actin depolymerizing factor/cofilin in dendritic organization and treadmilling of actin filament array in lamellipodia.* J Cell Biol, 1999. **145**(5): p. 1009-26.
84. Svitkina, T.M., et al., *Analysis of the actin-myosin II system in fish epidermal keratocytes: mechanism of cell body translocation.* J Cell Biol, 1997. **139**(2): p. 397-415.
85. Rouiller, I., et al., *The structural basis of actin filament branching by the Arp2/3 complex.* J Cell Biol, 2008. **180**(5): p. 887-95.
86. Volkmann, N., et al., *Structure of Arp2/3 complex in its activated state and in actin filament branch junctions.* Science, 2001. **293**(5539): p. 2456-9.
87. Welch, M.D. and R.D. Mullins, *Cellular control of actin nucleation.* Annu Rev Cell Dev Biol, 2002. **18**: p. 247-88.
88. Changede, R., et al., *Nascent Integrin Adhesions Form on All Matrix Rigidities after Integrin Activation.* Dev Cell, 2015. **35**(5): p. 614-621.
89. Plotnikov, S.V., et al., *Force fluctuations within focal adhesions mediate ECM-rigidity sensing to guide directed cell migration.* Cell, 2012. **151**(7): p. 1513-27.

Figure 1

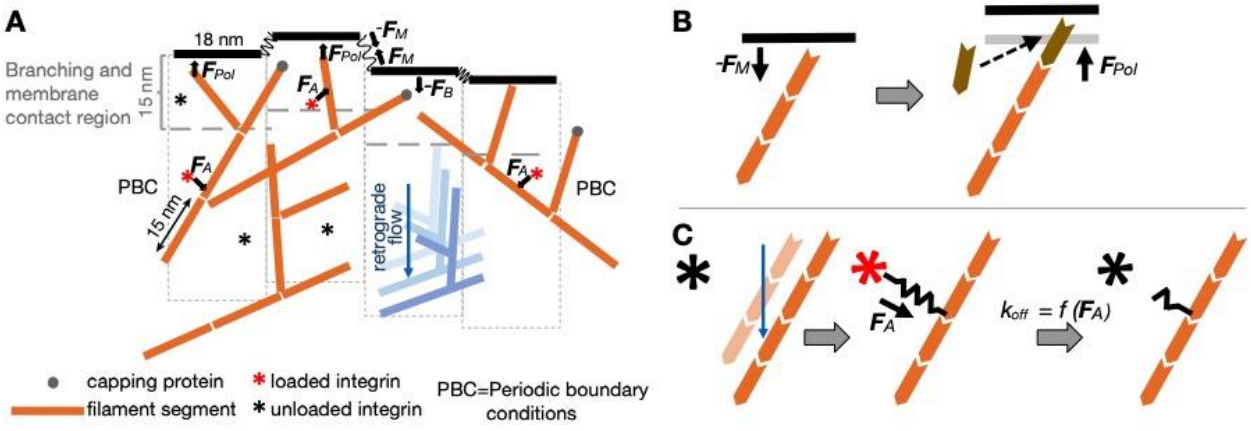

BR-MC model of lamellipodium protrusion. (**A)** Elements and interactions in the 2D computational model. Actin filaments are represented as polarized rigid rods of consecutive 15 nm units with each unit representing 5 actin monomers. Capping proteins bind the filaments with rate k_{cap} and prevent further polymerization. Each actin filament can form branches at a 70° angle within 15 nm from the edge membrane (k_{branch}). Polymerization with rate k_{pol} against the membrane pushes the membrane forward ($\boldsymbol{F}_{Pol}$). The membrane is represented as rods interconnected by harmonic potential energies with defined stiffness k_m , which create tension upon displacement, $\boldsymbol{F}_M$. A boundary force ($\boldsymbol{F}_B$) prevents the filaments from crossing the membrane. The membrane and boundary forces restrain actin polymerization and induce retrograde flow. Adhesions are represented as integrins that undergo cycles of activation and deactivation, with k_{on} and k_{off}, respectively. When active (black star), the adhesions connect actin filaments if within a proximity of 15 nm (red star). Adhesion engagement is represented as a spring and builds tension against the substrate in response to actin retrograde flow (adhesion tension, or traction force, $\boldsymbol{F}_A$). Adhesion density is maintained within the physiological range ~500 integrins/μm^2 [77]. A periodic boundary condition wraps the model edges and creates an infinite domain in which all the membrane segments experience spring tension on both sides.

For each time step, the new position for each actin filament is computed from the sum of Brownian forces, $\boldsymbol{F}_B$, $\boldsymbol{F}_M$, and $\boldsymbol{F}_A$. The new position for each membrane segment is computed from the sum of $\boldsymbol{F}_{Pol}$, $\boldsymbol{F}_M$, and $\boldsymbol{F}_A$. (**B)** The BR mechanism. Polymerized actin filaments (orange) undergo thermal motion in the 2D domain near the membrane. Addition of a new monomer (brown) against the membrane pushes the membrane outward with $\boldsymbol{F}_{Pol}$. (**C**) The MC mechanism. Actin undergoes retrograde flow (blue arrow) and integrins are activated (black star). Activated integrins bind to an actin filament to create adhesions with traction force ($\boldsymbol{F}_A$, red star) that slows the filament's flow and controls adhesion unbinding.

779 **Figure 2**

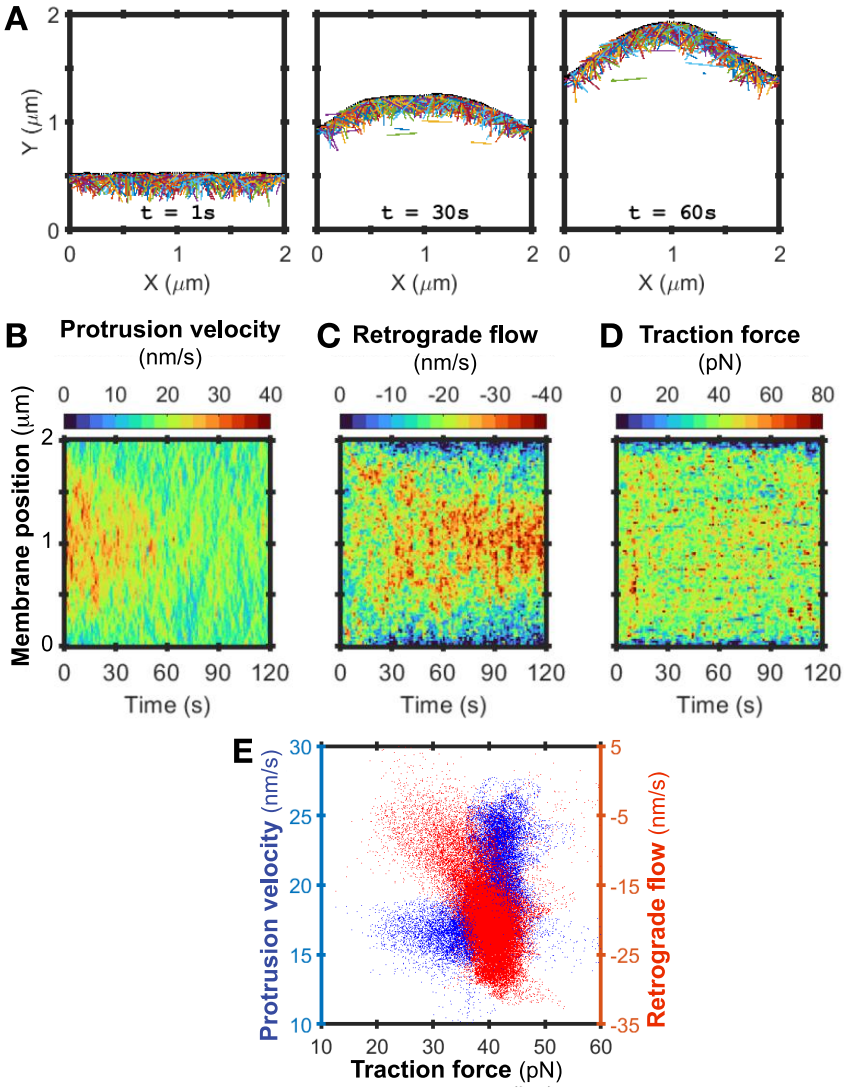

780

781 **Model reproduces physiological rates of edge protrusion and retrograde flow.**
782 (**A**) Snapshots from model simulations over run times in seconds (s). Individual filaments are
783 depicted in different colors. Parameters listed in Table 1. Membrane movement in Y from the
784 sum of forces (F_{Pol}, F_M, and F_A). (**B**) Heatmap of mean edge velocity at each 20 nm membrane
785 position (18 nm rod + 1 nm of spring on each side). 2 minute (min) simulation with k_m = 0.3
786 pN/nm, k_{branch} = 0.5 s^{-1}, k_{on} = 1 s^{-1}, k_{off} = 0.1 s^{-1}, and periodic boundary conditions. Sampling
787 every 0.001 s, averaged over 1 s intervals. Representative of n=10 iterations. (**C**) Heatmaps of

retrograde flow and (**D**) traction force, computed from simulations, sampling, and averaging as in B, and smoothening using a 2-D Gaussian filter with SD = 0.5. (**E**) Edge protrusion velocity and actin retrograde flow plotted as a function of traction force. Data from 3 model runs under conditions in B, but smoothened using a Gaussian smoothing kernel with standard deviation (SD) = 2. Points are values for individual membrane segments. Retrograde flow values within +/- 1000 nm/s were plotted, ≥ 94% of values.

Figure 3

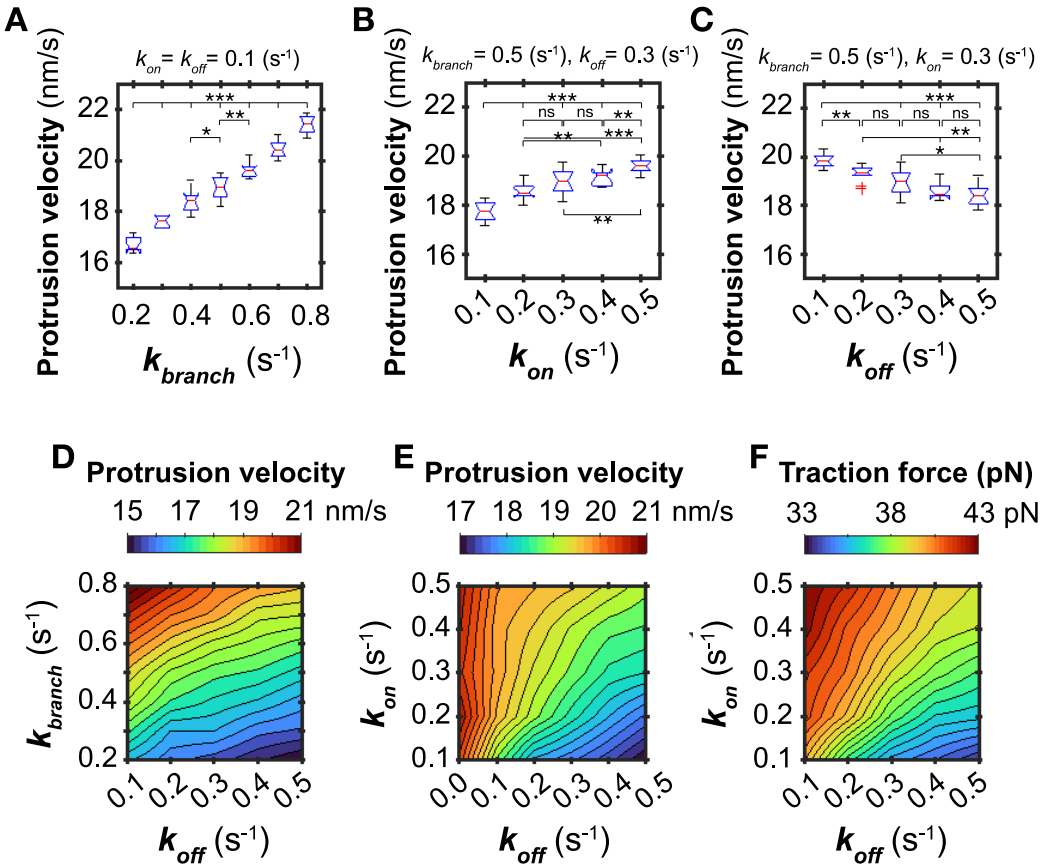

Actin assembly more significantly promotes protrusion velocity than adhesion assembly. (**A-C**) Distribution of lamellipodium velocity as a function of actin assembly rate k_{branch}, adhesion k_{on} and adhesion k_{off}. 10 s simulations with k_m = 0.3 pN/nm, maximum allowed adhesions = 1000 and periodic boundaries. Box plots' red line is median velocity and notches 95% CI, from n = 10 simulations. Significance is Mann-Whitney U test of mean. Adhesion density ranged around 500, (A) 493 - 505/μm^2, (B) 246 - 626/μm^2, (C) 758 - 378/μm^2. (**D**) Heatmap of mean protrusion velocity that results from variable actin k_{branch}, adhesion k_{on} = 0.1 s^{-1}, and variable adhesion k_{off}. (**E**) Mean protrusion velocity resulting from k_{branch} = 0.5 s^{-1} and variable k_{on} and k_{off}. (**F**) Mean traction force resulting from k_{branch} = 0.5 s^{-1} and variable k_{on} and k_{off}. Force computed from identical conditions as in A-E, except simulations were 20 s.

814 **Figure 4**

815

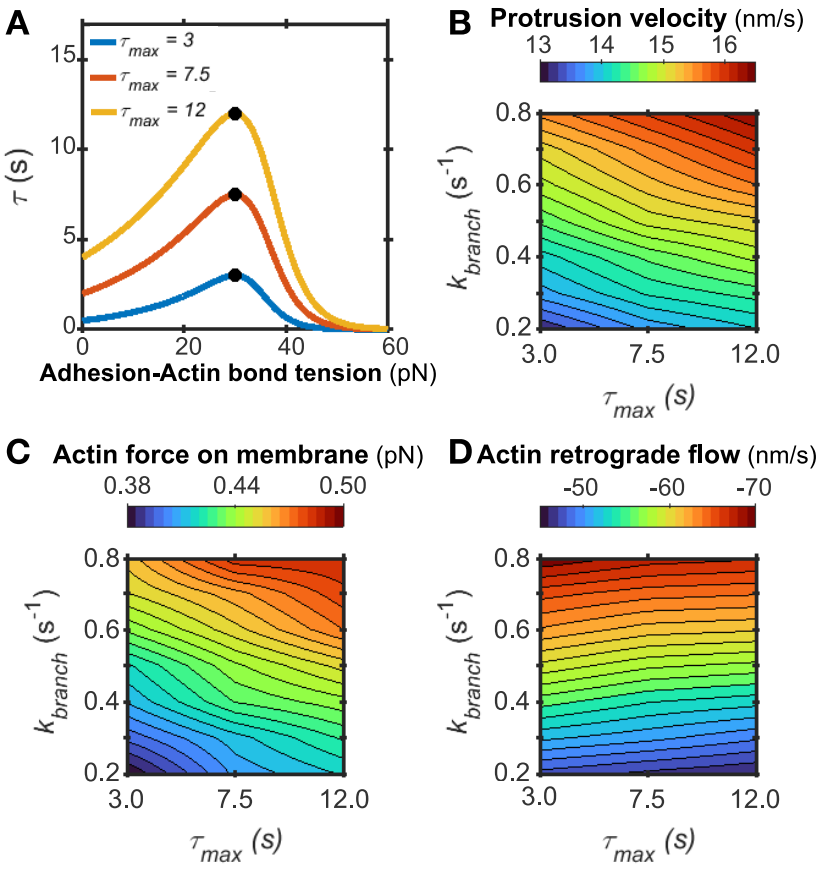

816

817

818 **The molecular clutch mechanism contributes to leading edge motion.** (**A**) Force-dependent

819 relationship of the molecular clutch: adhesion lifetime (τ) versus adhesion-filament bond tension

820 where $\tau = 1/k_{off}$. Under high tension (50 pN), k_{off} = 2 s^{-1} and k_{off} increases exponentially with

821 increased tension. (**B-D**) Mean protrusion velocity, actin force on membrane, and actin

822 retrograde flow velocity that results from variations in τ_{max} and k_{branch}. 10 s simulations with k_m =

823 0.3 pN/nm, k_{on} = 1.0 s^{-1}, molecular clutch engaged with τ_{max} = 3.0, 7.5, and 12.0 s with

824 intermediate values interpolated, maximum allowed adhesions = 2000, boundaries fixed, n = 10.

825 Because inactivated adhesions are removed from the modeling domain, k_{on} and the number of

826 allowed adhesions were increased to obtain 500 adhesions/μm^2 [77]. Membrane force calculated

827 as the mean membrane spring tension for all membrane springs and all time points. All flow
828 velocities are plotted.
829

Figure 5

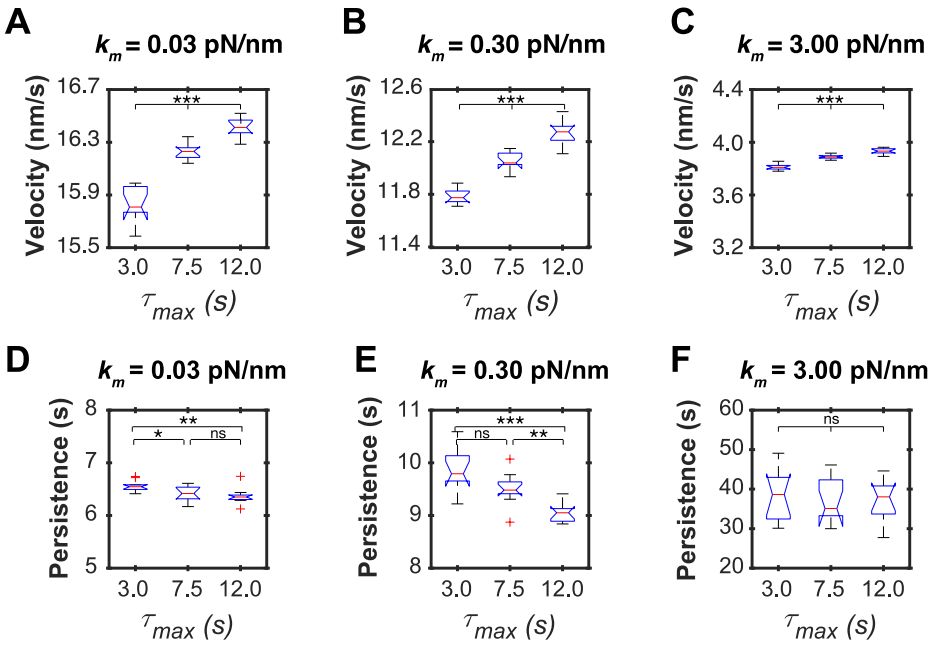

Adhesion lifetime promotes lamellipodia velocity but inhibits persistence. Model simulations in which membrane tension and molecular clutch τ_{max} varied, k_{branch} = 0.5 s^{-1}, k_{on} = 1.0 s^{-1}, boundaries fixed, 2 min run time. (**A-C**) Mean velocity measurements of the middle micron region of the membrane for each τ_{max} and each membrane tension. (**D-F**) Persistence measurements of the middle micron region of the membrane versus τ_{max} for each membrane tension. Persistence defined as the time between minimums in membrane segment velocities with minimums ≥ 5 nm/s. Box plots with red line marking medians and notches 95% CI. Significance is Mann-Whitney U test of means from n = 10 simulations.

843 **Figure 6**

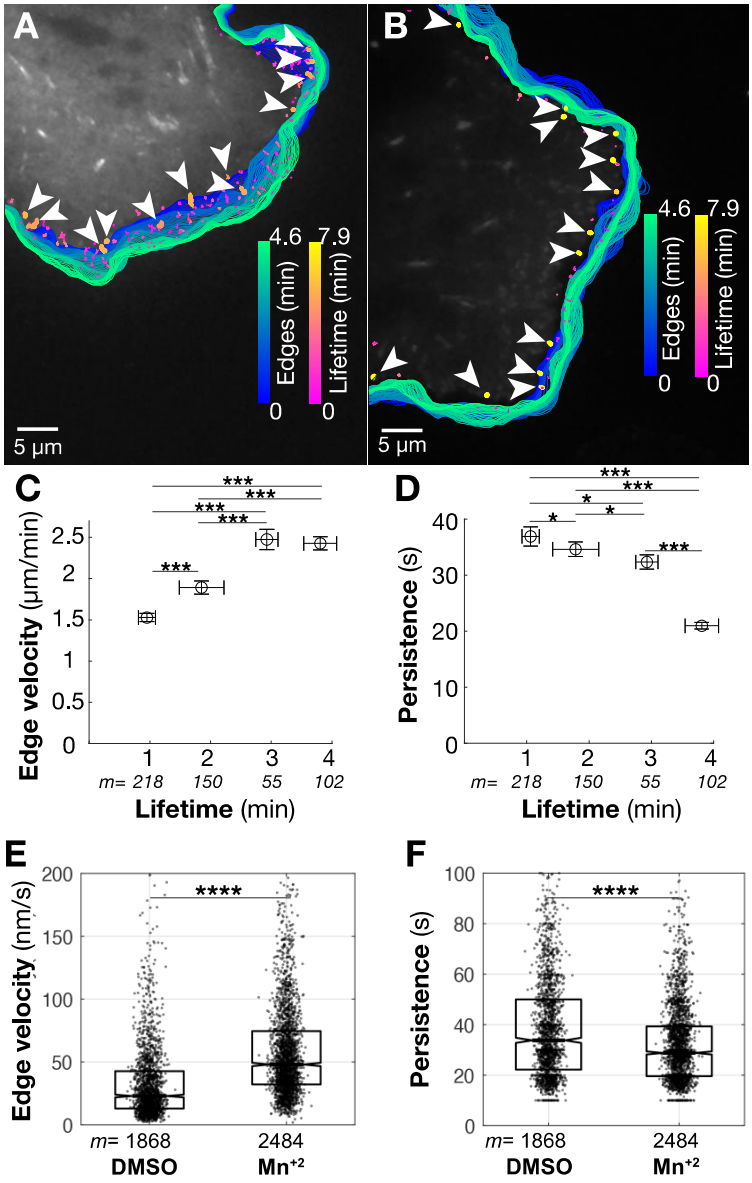

844

845 **Longer adhesion lifetime is associated with larger edge velocity and shorter persistence.**

846 (**A**, **B**) Tracked adhesions and segmented cell edges of COS7 cells with shorter lifetime (A) and

847 longer lifetime (B). Adhesions and cell edges are color-coded for lifetime and frame with $\Delta t = 3$

848 s, respectively. White arrowheads depict longer-living adhesions per each cell movie. (**C**) and

849 (**D**) Error bar plots of velocity (C) and persistent time (D) of edge protrusion in cells with

850 different overall lifetime. Error bar: standard error of mean. * $p<0.05$, *** $p < 10^{-15}$. *p* value

851 from Man-Whitney's U test. (**E, F)** Distribution of protrusion velocity (E) and persistence (F),

852 from *m* significant protrusion events in *n* = 7 cells treated with DMSO and *n* = 8 cells with

853 Mn^{+2}. Boxes span the 25^{th} to 75^{th} percentile. The central horizontal line is median and notches

854 are 95% CI. *p*

855 value from Kolmogorov–Smirnov test.

856

Table 1. List of model parameters

Model parameter name	Symbol	Default value	Reference
Time step	dt	*0.001 s*	
Actin Filaments			
Polymerization rate (barbed end)	k_{polym}	*13 s^{-1}*	[5, 78]
Depolymerization rate (pointed end)	$k_{depolym}$	*12 s^{-1}*	[79]
Branching rate (barbed end)	k_{branch}	*0.5 s^{-1}*	[43]
Capping rate (barbed end)	k_{cap}	*0.6 s^{-1}*	[80]
Filament force vector magnitude		*1 pN*	[81, 82]
Gamma (drag coefficient)	γ_F	*~0.01 pN s/nm*	
Filament mass threshold		*9000 units*	[5]
Average filament starting length		*225 nm*	[17, 60, 83, 84]
Filament unit length		*15 nm*	
Branch window height		*15 nm*	
Mean filament branch angle		*70 degrees*	[85-87]
Filament branch angle normal distribution SD		*10 degrees*	
Membrane			
Membrane spring constant	k_m	*0.3 pN/nm*	[41, 42]
Boundary force spring constant	k_b	*10 pN/nm*	
Gamma (drag coefficient)	γ_M	*0.1 pN s/nm*	
Membrane spring equilibrium length	$r_{0,M}$	*2 nm*	
Boundary spring equilibrium length	$r_{0,B}$	*0 nm*	
Membrane-filament contact region width		*15 nm*	
Segment width		*18 nm*	
Membrane length (at initialization)		*2000 nm*	
Adhesions			
Activation rate	k_{on}	*0.1-0.5 s^{-1}*	[31]
Deactivation rate	k_{off}	*0.1-0.5 s^{-1}*	[88]
Adhesion-filament spring constant	k_a	*10 pN/nm*	[24, 32, 74]
Adhesion-filament spring equilibrium length	$r_{0,A}$	*2 nm*	[89]
Filament connection threshold	r_{thresh}	*15 nm*	